

Highly nonlinear dipolar exciton-polaritons in bilayer MoS₂

Biswajit Datta^{1,*}, Mandeep Khatoniar^{1,2}, Prathmesh Deshmukh^{1,2}, Félix Thouin³, Rezlind Bushati^{1,2}, Simone De Liberato⁴, Stephane Kena Cohen³, and Vinod M. Menon^{1,2,*}

¹*Department of Physics, City College of New York, New York, NY, USA*

²*Department of Physics, Graduate Center of the City University of New York (CUNY),
New York, NY, USA*

³*Department of Engineering Physics, École Polytechnique de Montréal, Montréal, Quebec,
Canada*

⁴*School of Physics and Astronomy, University of Southampton, Southampton, UK*

*bdatta@ccny.cuny.edu, vmenon@ccny.cuny.edu

Abstract

Realizing nonlinear optical response in the low photon density limit in solid-state systems has been a long-standing challenge. Semiconductor microcavities in the strong coupling regime hosting exciton-polaritons have emerged as attractive candidates in this context. However, the weak interaction between these quasiparticles has been a hurdle in this quest. Dipolar excitons provide an attractive strategy to overcome this limitation but are often hindered by their weak oscillator strength. The interlayer dipolar excitons in naturally occurring homobilayer MoS₂ alleviates this issue owing to their hybridization of interlayer charge transfer exciton and intralayer B exciton. Here we demonstrate the formation of dipolar exciton polaritons in bilayer MoS₂ resulting in unprecedented nonlinear interaction strengths. A ten-fold increase in nonlinearity is observed for the interlayer dipolar excitons compared to the conventional A excitons. These highly nonlinear dipolar polaritons will likely be a frontrunner in the quest for solid-state quantum nonlinear devices.

Introduction

Photons are becoming ubiquitous in emerging quantum technologies like quantum communication and metrology due to the ability to propagate long distances while being robust against decoherence^{1,2}. To further extend the span of their utilities, platforms to achieve and implement strongly interacting photons in solid-state systems are highly desirable³. Conventional materials do not exhibit nonlinear response at power levels associated with single photons. In this context, remarkable advances have been made in cold atom systems to realize interacting photons at the single-particle level⁴. A strong contender for the generation of strongly interacting photons in the solid-state are exciton-polaritons formed via non-perturbative coupling of cavity photons with excitonic resonances. Although they can be modeled as non-interacting quantum fluids at low densities, beyond a critical density, saturation and short-range exchange interactions become significant and give rise to various phenomena like the appearance of spontaneous coherence, parametric down-conversion, and superfluidity⁵. Strong spatial confinement along with Coulomb interactions give rise to even stronger correlations between polaritons that can no longer be described using a mean-field theory. Such interactions give rise to non-Poissonian statistics of laser transmission, dubbed as polariton blockade. Preliminary evidence of such non-classical correlation was recently observed in confined polariton systems in GaAs^{6,7} but a small ratio of interaction to dissipation rates resulted in only a weak violation of classical correlations.

Transition metal dichalcogenides (TMDCs) have garnered much attention for their exceptional optoelectronic properties and have been used to demonstrate a wide array of fundamental phenomena and technological applications⁸. Furthermore, their two-dimensional (2D) nature allows for the formation of heterojunctions or homojunctions with arbitrary twist angles resulting in emergent properties⁹⁻¹². Their strong binding energy and large oscillator strength render them capable of forming polaritons at room temperature¹³, which has also been shown to retain the intriguing properties of the 2D excitons¹⁴⁻¹⁶. Polariton interactions in TMDCs under different configurations are being studied extensively. Realization of Fermi polarons¹⁷, trion polaritons^{18,19}, and excited-state Rydberg exciton-polaritons²⁰ have shown great potential in their abilities to harness strong polariton interactions. Moiré exciton-polaritons were recently demonstrated using heterobilayers of

WS₂/MoSe₂ where the electronic confinement potential arising from the twisted heterostructure was shown to enhance the nonlinearity⁹. However, all the platforms above rely on short-range exchange interactions or phase-space filling that pose a bottleneck in realizing few polariton non-linearity under current experimental capabilities.

In this context, a very attractive possibility is the use of spatially indirect interlayer excitons (IE) in TMDC heterostructures²¹ that can have a permanent dipole moment and hence support highly interacting dipolar polaritons. Formation of polaritons with excitons that possess a permanent dipole moment has been shown to enhance the polariton interactions both in resonant^{22,23} and non-resonant excitation schemes²⁴. However, their inherently low oscillator strength creates an impediment in reaching the strong coupling regime without hybridization with a direct intralayer exciton. Furthermore, the large in-built interfacial electric fields make electrical tuning of the energies of the IE far more difficult. Bilayer MoS₂ provides a highly attractive platform to solve these issues²⁵⁻²⁸. The IE in naturally stacked 2H bilayer MoS₂ remarkably has both an out-of-plane (static) dipole moment and an in-plane (oscillating) dipole moment. Due to the in-plane dipole moment, the IE in MoS₂ bilayer has an oscillator strength of approximately 36% of that of the intralayer A exciton along with strong absorption that is visible up to room temperatures. Moreover, a strong response to DC electric fields has been demonstrated in these systems, thus confirming their dipolar nature^{25,26,28}. In this work, we achieve a strong coupling of microcavity photons with the IEs (along with intralayer A and B excitons) in bilayer MoS₂. The IE polariton shows 10 fold enhancement of the polariton nonlinearity compared to the intralayer A exciton owing to its dipolar and phase space filling contributions. Such enhanced nonlinear response makes them appealing to realize strongly interacting polaritons in condensed matter systems. In addition, the ease of fabrication and realization of multi-polariton species in this system makes it a practical and fundamentally interesting material for studying polariton physics.

Results

Fig. 1a shows a schematic of the bands that form interlayer exciton (IE) in bilayer MoS₂. IE₁ and IE₂ excitons in which electrons are in layer 1, and layer 2 respectively, are energetically degenerate at zero external bias while the hole is delocalized among both layers. The black arrows in Fig. 1a indicate

the transitions that form the IE. This peculiar charge distribution is at the heart of producing both in-plane and out-of-plane dipole moments of IE. Fig. 1b shows the charge distribution in real space for IE_1 and IE_2 . Owing to the spatial separation of the electron and the hole, it acquires a permanent dipole moment, the nature of which has been a topic of much interest recently ^{25–28}. IEs in MoS_2 homobilayer can be thought of as an admixture of B intralayer exciton with an optically dark but electric field tunable charge-transfer exciton, which is typically found in TMDC heterobilayers²⁹. As a result, IEs in MoS_2 homobilayer acquire both a strong oscillator strength and electric field tunability ²⁹. Fig. 1c shows the white light differential reflection of the bilayer sample at zero power limit at 7 K. The peaks at 1.9365 eV, 2.000 eV, and 2.1076 eV correspond to the A, IE, and B excitons, respectively. Interestingly, the absorption of the IE is prominent even at room temperature, which provides a straightforward method to identify the MoS_2 bilayer flakes after mechanical exfoliation (see SI Fig.S3).

We probe the nonlinear optical response of the IE and A exciton using resonant pump experiments (see Methods). The relative shift of A exciton and IE so obtained are plotted in Fig. 1d against the estimated density of A exciton and IE, respectively (see Methods for the details of the exciton density calculation). Both the excitons blueshift with increased excitation density, with the IE shift being more pronounced. Exchange interaction is the dominant mechanism responsible for the blue shift for the A exciton, while dipolar interactions dominate the interaction in the IE response as exchange interaction is likely to be small given the larger spatial separation of electron and holes³⁰. To better understand the exciton dynamics, we have also performed ultrafast pump-probe spectroscopy on the bilayers (see SI section X for the pump-probe data). In this case, the spectra show a redshift of the resonances accompanied by a nearly identical transient response regardless of which exciton is first pumped (A, IE or B). This can be understood if carriers rapidly relax out of the K valley to the band minima on a scale faster than the ~ 200 fs time resolution. This supports our hypothesis that the A and IE transitions are nearly homogeneously broadened with a lifetime dictated by the intervalley scattering rate. This agrees well with recent coherent spectroscopy and numerical calculations performed for bilayers of $MoSe_2$ ³¹. The above approach is used to estimate the exciton density in Fig. 1d.

Exciton polaritons were realized in the bilayer MoS_2 by embedding it in a microcavity. Fig. 2a shows the schematic of the structure used in this experiment. It consists of a bilayer MoS_2 encap-

sulated by thin (20 nm) hexagonal boron nitride (hBN), which is sandwiched between a bottom dielectric distributed Bragg reflector (DBR) mirror and a top silver mirror. See SI Note I and Methods for the fabrication details and cavity structure. The cavity is designed such that the bilayer MoS₂ flake sits close to an electric field anti-node, allowing us to observe five dispersive modes associated with the different polaritonic states as shown in Fig. 2b. These distinct polariton modes arise due to the hybridization of the cavity photon mode with the various excitonic states present in the bilayer system. We name the polariton branches as pol-1 through pol-5, with pol-1 corresponding to the lowest energy and pol-5 the highest. From the Fig. 2b, we see that the 1s state of A, the IE, B exciton and 2s Rydberg state of A exciton all strongly couple to the same cavity mode at 7 K. We fit the data with a five-coupled oscillator model where the energy of all the four excitons, the cavity mode, their Rabi splitting, and the effective refractive index of the system are treated as fit parameters. The fit results in exciton energies $E_{A1s} = 1.9323 \pm 0.0003$ eV, $E_{IE} = 2.0014 \pm 0.0001$ eV, $E_{A2s} = 2.078 \pm 0.002$ eV, $E_B = 2.111 \pm 0.001$ eV and the Rabi splittings $\Omega_{A1s} = 40.4 \pm 0.3$ meV, $\Omega_{IL} = 21.4 \pm 0.1$ meV, $\Omega_{A2s} = 13 \pm 0.5$ meV, $\Omega_B = 51 \pm 0.4$ meV. The exciton energies obtained through the fit agree well with the experimentally determined exciton energies with slight shifts due to the strain and changes in the dielectric environment in the cavity. In our device, the bare cavity mode is positively detuned from the A_{1s} exciton by $\delta_{C-A_X} = 17$ meV. See SI Note II for details on the coupled oscillator model. Fig. 2c shows the line cuts of the full k-space data at three different k_{\parallel} where the cavity mode is resonant with the A exciton (yellow), IE (red) and B exciton (blue), respectively. We notice that the Rabi splitting of the IE polariton remains observable even at 77 K (see SI Fig.S3).

We measured the white light reflectivity at the IE and A resonance and monitor the energy shifts of the polariton branches, see SI Note V and SI Note VIII for the details of the experiment. Fig. 3a shows the energy of the upper and lower branch of the IE polariton as a function of polariton density at the inplane wavevector corresponding to the zero-detuning k_{\parallel} (where the cavity mode and exciton energy are degenerate). Two Lorentzian fits at each density is used to obtain the energy of the upper and lower polaritons. SI Note IV discusses the details of the polariton density calculation and SI Note V provides the raw data of the density dependent differential reflection of IE polariton. We can see from Fig. 3 that the lower branch of the IE polariton moves with pump power more than the upper branch. We also observe a simultaneous increase of the the magnitude of zero-detuning

k_{\parallel} along with the reduction of Rabi splitting. This suggests the presence of both exciton energy renormalization and saturation effect. SI Note VII shows the density-dependent Rabi splitting of IE polariton. Taking the derivative of the E_{LP} with respect to density, we calculate the strength of the nonlinearity, g_{LP} . Since the rate of blue shift saturates at high density (olive curve in Fig. 3a), g_{LP}^{IE} reduces with polariton density as seen in Fig. 3b. Note that at the lowest powers accessible in our measurement, the IE lower polariton branch already shows a power-dependent blueshift. On the other hand, within the accessible range of the polariton density in our experiment, g_{LP}^A remains nearly a constant (see SI Note VIII for the blueshift data of the lower polariton branch of A exciton). The obtained strength of the non-linearity in the low density limit for IE and A exciton polaritons are $g_{LP}^{IE} \sim (100 \pm 2) \mu\text{eV } \mu\text{m}^2$ and $g_{LP}^A \sim (10 \pm 0.2) \mu\text{eV } \mu\text{m}^2$ respectively corresponding to 10 fold increase in the nonlinear response for the IE polaritons.

Discussion

We note that the g_{LP}^A value is comparable to the previous report for A exciton-polariton in monolayer TMDCs^{20,32}. This allows us to compare the nonlinearity of the IE in bilayer MoS₂ with that of Rydberg A_{2s} state reported in ref.²⁰ – we find that the nonlinear response of IE is even larger than the A_{2s} state by a factor of ~ 2.7 . More importantly, we would like to highlight a few critical differences between these two studies. The approximately 4 times enhancement in the g_{LP} for A_{2s} state in ref.²⁰ is attributed to the enhanced phase-space filling due to a higher Bohr radius of 2s compared to 1s. However, this enhancement in nonlinearity comes at the cost of reduced oscillator strength. This is overcome in ref.²⁰ by stacking three layers of monolayer TMDC separated by thin hBN. There is, however, no clear experimental route towards using higher-order Rydberg states beyond $n > 2s$ in TMDCs to get even higher enhancement as the oscillator strength almost vanishes for higher-order Rydberg states. Additionally, the higher-order Rydberg states are also more susceptible to disorder due to their larger Bohr radius. On the other hand, the spectral signature of interlayer exciton in bilayer MoS₂ is visible even at room temperature and was shown to have a significant response to applied out of plane electric field²⁵. This provides a platform with the possibility of creating highly interacting dipolar polaritons controlled by external electric fields.

Nonlinear polariton interactions in the present case have contributions from exciton-exciton

Coulomb interaction (which includes both dipolar and exchange terms) and phase space filling effect. For intralayer excitons with a small Bohr radius only the exchange term and phase space filling effect is important³⁰. On the other hand, for interlayer excitons in traditional quantum well systems, the direct dipole-dipole interaction dominates, and the exchange interaction is neglected due to the separation between charges in the two layers³³. In contrast in MoS₂ homobilayers, the hole is delocalized across the two layers, and hence there is a finite overlap with the electron wavefunction leading to small but non-zero exchange interactions. Thus in the present experiments, in addition to the saturation effects, both dipolar and exchange interaction contribute to the overall nonlinear response, with the latter being less significant owing to the finite separation between the electron and hole.

To discern the contributions to the polaritonic nonlinearity due to dipolar and exchange interaction of excitons ($\Delta E_{\text{exc-exc}}$) versus phase space filling (ΔE_{sat}) we carry out the following analysis. Fig. 4a shows the Hopfield coefficients of all the excitonic components and the cavity photon as a function of k_{\parallel} . This is used to obtain the shift in polariton energy, $\Delta E_{\text{LP}}^{\text{IE}}$ as a function of Hopfield cavity photon fraction (C), see Fig. 4b. The interaction strength due to phase space filling can be written in terms of $g_{\text{LP}} = 4g_{\text{SAT}}|C||X|^3$, where X is the Hopfield coefficient for the exciton. Although this is a multi-exciton system, the contribution of the other excitons close to the zero-detuning k_{\parallel} of the IE is small. Thus, we can write $g_{\text{LP}}^{\text{IE}} = 4g_{\text{SAT}}|C|(1 - |C|^2)^{3/2}$ which is a non-monotonic function of the cavity Hopfield coefficient as shown in the Fig. 4b inset (red curve). For the case of exchange and dipolar interaction, the interaction strength scales as $g_{\text{LP}} = g_{\text{XX}}|X|^4 = g_{\text{XX}}(1 - |C|^2)^2$ ^{23,33} which monotonically decreases with increasing $|C|$ (cyan curve in Fig. 4b inset). We find that the measured nonlinear response of the IE polariton is the highest at an in-plane wave vector larger than zero-detuning k_{\parallel} , as seen in Fig. 4b. We also notice that $\Delta E_{\text{LP}}^{\text{IE}}$ changes non-monotonically with the cavity Hopfield coefficient. The tilted parabolic shape of the measured $\Delta E_{\text{LP}}^{\text{IE}}$ as a function of $|C|$ indicates a roughly equal contributions from both $\Delta E_{\text{exc-exc}}$ and ΔE_{sat} .

Fig. 4c shows a schematic of the polariton energies at two different powers for $\Delta E_{\text{sat}} > \Delta E_{\text{exc-exc}}$. Due to both the blue shift of the exciton and saturation effect, the lower branch moves with increasing power more than the upper branch. Analyzing the blueshift of the IE lower polariton branch and redshift of the IE upper polariton branch at the zero-detuning k_{\parallel} we calculate the magnitude of $\Delta E_{\text{exc-exc}}$ and ΔE_{sat} in our system. At the zero-detuning k_{\parallel} we write the energy shift of IE

lower branch as $\Delta E_{\text{LP}}^{\text{IE}} = \Delta E_{\text{exc-exc}} + \Delta E_{\text{sat}}$ and the energy shift of IE upper branch as $\Delta E_{\text{UP}}^{\text{IE}} = \Delta E_{\text{exc-exc}} - \Delta E_{\text{sat}}$. From these equations we obtain $\Delta E_{\text{exc-exc}}$ and ΔE_{sat} as a function of polariton density, see SI Note IX. The ratio of $\Delta E_{\text{sat}}/\Delta E_{\text{exc-exc}}$ as a function of polariton density is shown in Fig. 4d, indicating that the magnitude of the dipole mediated exciton-exciton interaction non-linearity and saturation nonlinearity are comparable especially at low polariton densities. Further increase of dipole-dipole interaction by creating imbalance between up and down dipoles (via applied electric field or providing strain) will allow to access regime where dipolar interactions dominate.

We now discuss the origin of the net dipolar interaction arising in our system at the zero electric field. The two ground states of the interlayer exciton are quasi degenerate at the zero electric field and should not possess net dipole moment in an ideal limit. However, as our experiments indicate, dipolar interactions play a crucial role in the 10 fold enhancement in interaction strength we observe for the interlayer exciton-polaritons. This raises questions about the origin of the dipole moment. Structural asymmetry, strain, residual electric fields, and disorder are the likely reasons for breaking the symmetry and resulting in a net dipole moment. Given that the bilayer MoS₂ is sandwiched between two hBN layers of similar thickness, one can rule out the role of structural asymmetry. While local strain and built-in fields could have highly localized effects, we observed similar enhancement over the entire bilayer sample, and hence one can conclude that local strain or fields are also not the key contributors. Finally, if one looks at disorder arising from defects present in the 2D TMDCs, the typical defect densities observed in mechanically exfoliated monolayer MoS₂ is on the order of 10^{12} - 10^{13} cm⁻² as has been shown before³⁴. Using the lower bound of 10^{12} cm⁻² we can estimate the lower bound for dipolar interaction arising from local symmetry breaking between the two layers of the bilayer system. Using a Poisson distribution of defects, we estimate 36% of the carriers in one layer see a defect in its vicinity, thereby introducing a net dipole moment. This effect has been hypothesized to be the reason behind the observation of a sizable second harmonic generation in bilayer MoS₂ even at zero perpendicular DC electric field³⁵. This local imbalance of the up and down dipole moment will increase the dipole-dipole interaction observed in our experiment.

In summary, we demonstrate extremely large optical nonlinearity arising from IE polaritons in homobilayer MoS₂. The reported nonlinearity is an order of magnitude larger than that reported for the A excitons in TMDCs, bringing the IE polaritons closer to the polariton blockade regime.

The enhanced nonlinear response of the exciton-polaritons is attributed to the dipolar interaction of the interlayer excitons and the saturation nonlinearity with the former starting to dominate in the weak pump limit. The homobilayer MoS₂ system presents itself as an attractive platform to realize IE polaritons without the need for precise twist angle control while having the potential to reach elevated operational temperatures. Using an electric field to induce preferential dipole moment along with lateral photon confinement in the microcavity is expected to push the bilayer MoS₂ polariton system into the quantum nonlinear regime.

Methods

Fabrication details

The DBR used in our experiment is made of 8 pairs of SiO_2 (104.9 nm) and TiO_2 (64.7 nm) layers and were deposited by radio frequency sputtering on an intrinsic Si chip. MoS_2 and hBN were exfoliated from bulk crystals (from 2Dsemiconductor Inc.) using blue tape (Nitto) and scotch tape respectively. MoS_2 was exfoliated onto PDMS substrate and hBN was exfoliated onto a 300 nm SiO_2/Si substrate. Bilayer MoS_2 flakes were identified by reflection spectroscopy – the additional dip at ~ 639 nm in the reflection signal at room temperature is the hallmark of bilayer MoS_2 . hBN/bilayer MoS_2 /hBN heterostructure stacking and transfer were done using the well-known polypropylene carbonate transfer technique³⁶. The chosen top and bottom hBN layers were of similar thickness ~ 20 nm. The final stack was then transferred onto the DBR at a temperature of 150°C . The chip was kept in chloroform for 12 hours to remove the polypropylene carbonate residue. 240 nm polymethylmethacrylate (PMMA) (495 A4 from Microchem) was spin-coated to form a $3\lambda/2$ cavity. Finally, a silver layer (40 nm) was deposited by electron-beam evaporation for the top mirror of the microcavity. Optical images of the device and the bare cavity response are given in SI Note I.

Optical measurement details

We recorded the angle-resolved reflection spectra using the Fourier space imaging technique. A broadband halogen light source was used for reflection measurements. A supercontinuum pulsed light source (NKT Photonics, repetition rate 80 MHz, pulse duration 20 ps) was used to study the power dependence of the bare excitons and polaritons. Appropriate long pass and short pass filters were used in the input to excite a narrow band around the excitons/polaritons under study. For the IE polariton, the excitation bandwidth of the supercontinuum laser was chosen to be ~ 40 meV around the IE energy in the power-dependent measurements. The set-up was coupled with a Princeton Instruments monochromator with a CCD camera. A 50X, 0.65 numerical aperture objective was used for all the measurements at 7 K in a closed cycle Montana cryostat. The polariton dispersion was revealed by imaging the back aperture of the microscope objective (Fourier plane) onto the camera. The spot size of the laser was $1 \mu\text{m}^2$ on a uniform area of the sample of

dimension $\sim 500 \mu\text{m}^2$.

Exciton density calculation in the absence of the top mirror

For the data presented in Fig.1d, we excite A, IE and B exciton simultaneously at various optical fluences. We have used a supercontinuum laser with a 20 ps pulse width and broadband excitation (1.907 eV to 2.246 eV) scheme for this measurement. At all fluences, each spectrum is fitted with the sum of three Lorentzians to track the evolution of each feature with excitation fluence (see SI Note VI). To calculate the density of individual excitons, we do the following.

We first calculate the absorbed power density by the bilayer MoS₂

$$P_{\text{absorbed}} = \frac{\int_{E_{\text{min}}}^{E_{\text{max}}} P_{\text{laser}}(E)L(E - E_X)dE}{A_{\text{beam}}} \quad (1)$$

Here $P_{\text{laser}}(E)$ is the intensity profile of the incident supercontinuum laser, $L(E - E_X)$ is the absorbance of X exciton around its energy E_X , and A_{beam} is the size of the focused laser beam on the sample. We run the integration within 74 meV (53 meV) band around the A exciton (IE) peak energy, respectively. Beyond these bands, the reflection contrast of A exciton and IE are not detectable. The absorbed photon density from the absorbed power density is calculated taking into account the life time of these excitons (45 fs for A exciton 53 fs for IE). We assume all of the absorbed photons form excitons.

Transient reflectivity measurements

Transient reflection spectroscopy measurements presented in SI Note X were obtained using an ultrafast transient absorption spectrometer (Harpia, Light Conversion). An ultrafast optical parametric oscillator (Orpheus-F, Light Conversion) provided the pump pulses and white light continuum generation in a sapphire crystal provided the probe pulse. These were filtered using a pinhole inside a telescope and collinearly sent to a home-built microscope equipped with a 50x objective (NA 0.45). The sample was held at 3.5 K using a closed-cycle cryostat (Montana Instruments) overlooked by the microscope. The output lens of the filtering telescope was adjusted to obtain pump and probe spots as large as the bilayer flake. Before its detection by a spectrometer, the pump was removed

from the light reflected by the sample using a polarizer so that only the probe beam was detected.

Error in estimating density of polaritons

Currently, the density error bars consider the error in measuring power, determining the energy and linewidth of the polariton. However, one primary source of the error is the lifetime of the polaritons. To address this issue we have done pump-probe experiment which validates the use of the linewidth of the polaritons to determine the polariton lifetime. Results of our pump-probe experiment is included in the SI note X. Another likely source of error is estimating efficient photons' loading into a cavity. This is because the conventional input-output theory does not account for lossy mirrors, as in our experiment. Also photon loading into microcavities from free space is not efficient due to mode mismatch between the free space laser modes and bi-orthonormal modes in lossy cavities³⁷. However, the relative enhancement of the nonlinearity of IE with respect to A remains unaffected due to the above errors as they exist for both the IE and A exciton polariton.

Acknowledgements

We acknowledge support from ARO through grants W911NF-17-1-0312 and W911NF-22-1-0091; NSF DMR-2011738, and AFOSR-FA2386-21-1-4087. The low temperature spectroscopy facility was supported by NSF MRI grant - DMR-1726573. S.D.L. acknowledges support from a Royal Society Research Fellowship and from the Philip Leverhulme Prize of the Leverhulme Trust.

Contributions

V.M.M., M.K. and B.D. conceived the experiments. B.D. fabricated the device. R.B. helped in the fabrication. B.D., M.K. and P.D. performed the measurements. F.T. did the time resolved pump probe measurements. B.D. did the data analysis with inputs from M.K., P.D. and V.M.M. S.D.L. and S.K.C. gave inputs in the data interpretation. B.D, M.K. and V.M.M wrote the manuscript with comments from all authors.

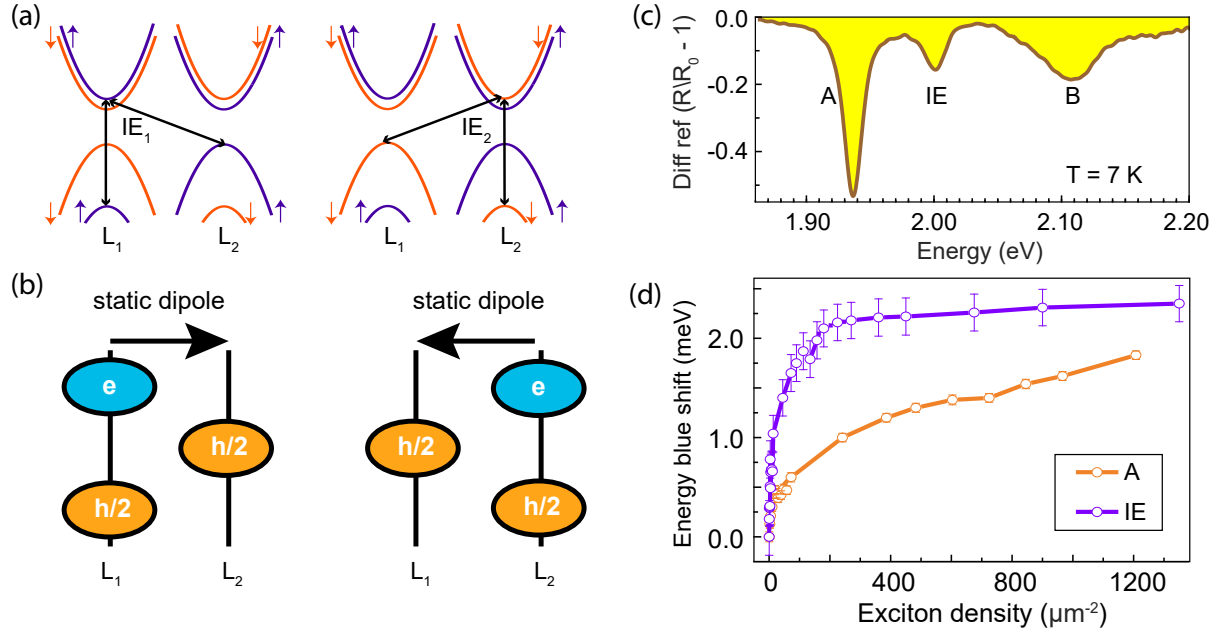


Fig. 1: Excitons in MoS₂ bilayer and white light absorption. (a) Schematic of the band structure (around the K point) of the bilayer MoS₂ showing (black arrows) the participation of the different bands in the IE formation. The blue and red colors represent the up and down spin, respectively. L₁ and L₂ refer to the layer 1 and layer 2 of the bilayer MoS₂, respectively. (b) Schematic showing the two possible charge configurations in the absence of bias voltage between the two layers. In both cases, the electron is localized in one of the layers, and the hole is distributed among both the layers. (c) White-light differential reflection at 7 K showing three dips corresponding to A, IE, and B exciton, respectively. (d) Relative shift of excitonic features observed in instantaneously-probed pulsed reflectivity with increasing exciton density. Pulse duration = 20 ps. The K valley lifetime of A exciton (45 fs) and IE (53 fs) estimated from their respective linewidths are used to estimate the exciton density from the pump fluence. The error bars represent the variance of the fitted parameters caused by noise in the measurement.

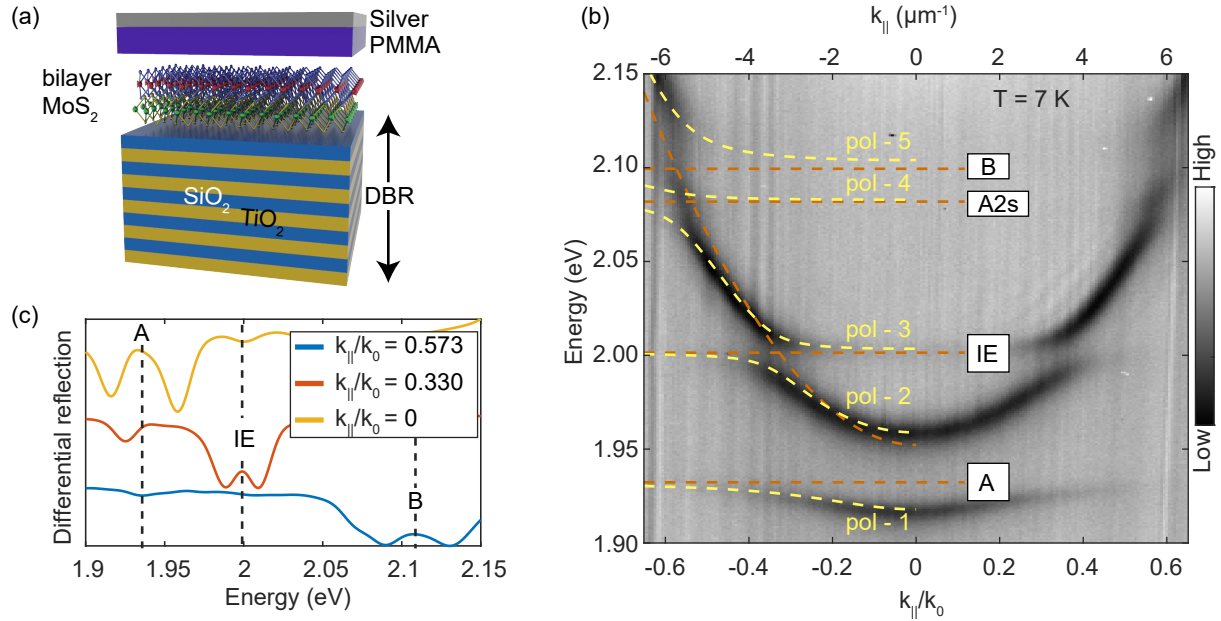


Fig. 2: Device schematic and polariton dispersion. (a) Schematic of the device. The bilayer MoS₂ is sandwiched between two hexagonal boron nitride flakes of almost similar thickness ~ 20 nm. The entire stack is transferred by the polypropylene carbonate (PPC) method onto a SiO₂ terminated SiO₂-TiO₂ DBR. As the cavity spacer, a layer of 240 nm thick PMMA was spin-coated on the stack. Finally, 40 nm of Ag was deposited via electron beam evaporation to form a $3\lambda/2$ cavity, where λ is the cavity resonance wavelength. (b) White light differential reflection showing all branches of the polaritons at 7 K. 1s and 2s states of A exciton, IE, and B exciton all are strongly coupled to the same cavity mode. This data was measured by illuminating the sample with incoherent halogen light with a power of few nW at the sample. The yellow dashed lines are the polariton eigenvalues obtained from fit using the five coupled oscillator model. The brown dashed lines denote the energy of the excitons and the cavity mode resulting from the fitting. Here $k_0 = \frac{2\pi}{\lambda_c}$; λ_c is the wavelength of the uncoupled cavity mode at $k_{||} = 0$. (c) Line cuts at different $k_{||}$ of the color plot shown in panel-b. It clearly shows that each exciton strongly couples, resulting in two polariton modes that lie above and below the excitonic resonances.

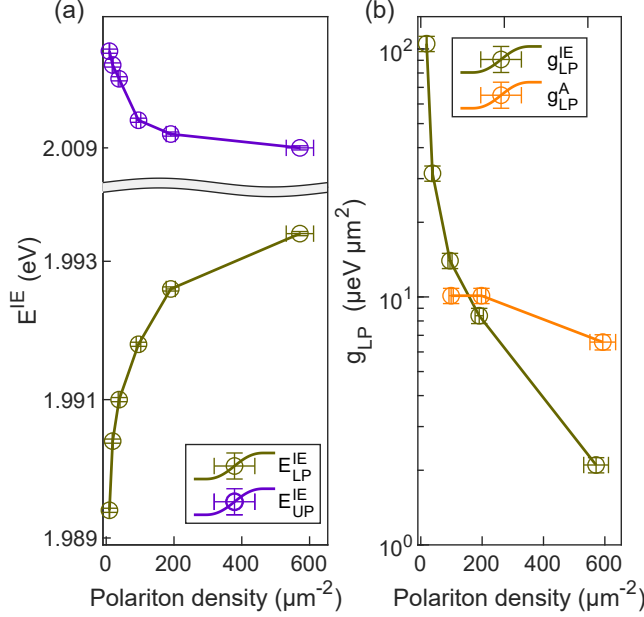


Fig. 3: Comparison of nonlinearity of the IE polariton with A exciton polariton. (a) Energy of the lower and upper branch of the IE polariton as a function of the polariton density at zero-detuning k_{\parallel} . The movement of the lower branch is more than the upper branch due to the combined effect of exciton-exciton interaction and saturation. The error bars in energy represent the uncertainty in determining the peak of the Lorentzian fit (polariton energy) to the reflection data. (b) $g_{\text{LP}}^{\text{IE}}$ (g_{LP}^{A}) as a function of the IE (A) lower branch polariton density at zero-detuning k_{\parallel} . g_{LP} is defined as the local slope of the polariton energy vs. polariton density graph. $g_{\text{LP}}^{\text{IE}}$ and g_{LP}^{A} are calculated from the lower branch of A polariton and IE polariton, respectively. Note that the g_{LP} of IE polariton $\sim (100 \pm 2) \mu\text{eV } \mu\text{m}^{-2}$ is almost 10 times larger than the g_{LP} of A exciton polariton $\sim (10 \pm 0.2) \mu\text{eV } \mu\text{m}^{-2}$. All the power-dependent nonlinear measurements were carried out using a pulsed supercontinuum laser (20 ps pulsewidth) with proper bandpass filter in the input to excite only one polariton species. The polariton density corresponds to the specific branch being excited. The density error bars take into account the error in measuring power and determining the energy of the polariton and linewidth from the Lorentzian fits. The error bars in g_{LP} consider the error in determining the density and the energy of the polariton.

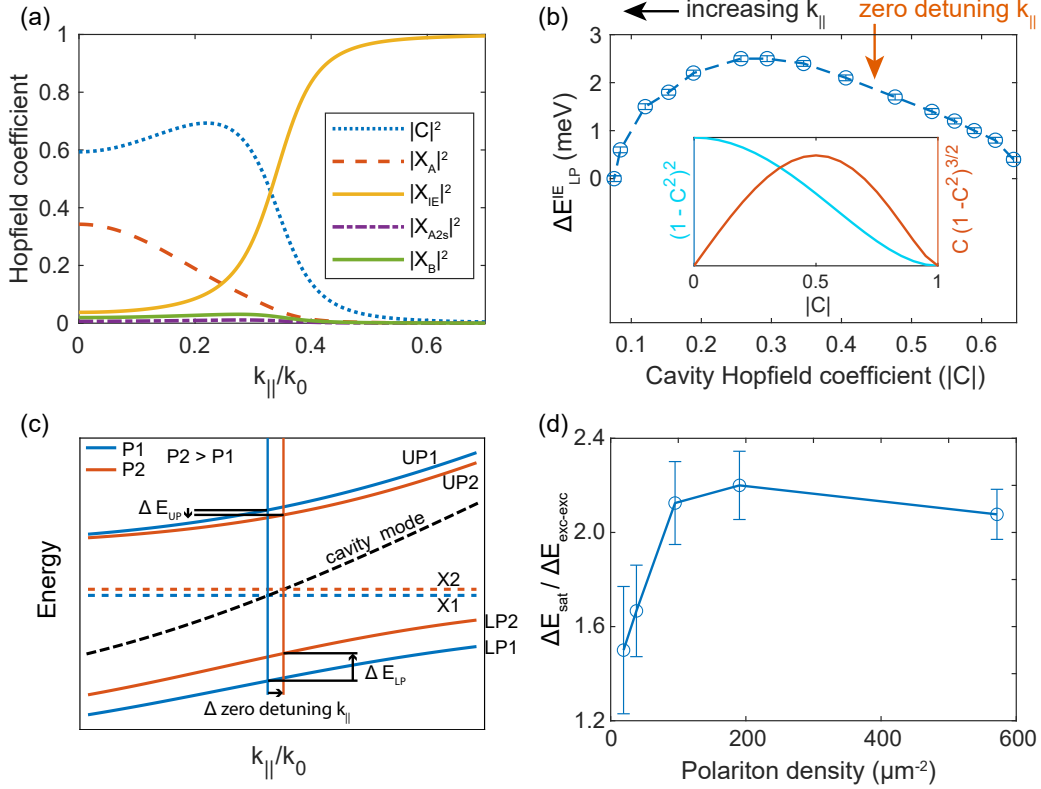


Fig. 4: Nonlinear response of the IE polariton. (a) The Hopfield coefficients of the lower IE polariton showing the contributions of cavity photon and the four excitons as a function of k_{\parallel} . (b) Experimentally measured blueshift of the IE lower branch as a function of k_{\parallel} at a polariton density $\sim 95 \mu\text{m}^{-2}$. Here k_{\parallel} is converted to cavity Hopfield coefficient using the previous plot. The blueshift of the lower branch of IE (ΔE_{LP}^{IE}) is highest close to the zero-detuning k_{\parallel} , but the shape looks like a tilted parabola. This can be explained by taking both exciton-exciton interaction and saturation effect into account. Inset shows the theoretically expected dependence of exciton-exciton interaction and saturation effect on $|C|$. It can be seen that superimposition of these two graphs can explain the tilted parabola shape of ΔE_{LP}^{IE} in our data. (c) Cartoon showing the IE polariton dispersion at two different excitation powers where the combined effect of exciton-exciton interaction and saturation effect is present. Here, X_1 and X_2 are the exciton energies at power P_1 and P_2 , respectively. The zero-detuning k_{\parallel} increases with increasing power since the exciton blueshifts. Due to the combined effect of exciton blueshift and saturation, the lower IE polariton branch moves more than upper IE polariton branch. (d) Ratio of estimated saturation nonlinearity and exciton-exciton interaction nonlinearity as a function the IE lower branch polariton density. The error bars in energy represent the uncertainty in determining the peak of the Lorentzian fit (polariton energy) to the reflection data.

References

- [1] Gisin, N. & Thew, R. Quantum communication. *Nature photonics* **1**, 165–171 (2007).
- [2] Giovannetti, V., Lloyd, S. & Maccone, L. Quantum-enhanced measurements: beating the standard quantum limit. *Science* **306**, 1330–1336 (2004).
- [3] Chang, D. E., Vuletić, V. & Lukin, M. D. Quantum nonlinear optics—photon by photon. *Nature Photonics* **8**, 685–694 (2014).
- [4] Lukin, M. D. *et al.* Dipole blockade and quantum information processing in mesoscopic atomic ensembles. *Phys. Rev. Lett.* **87**, 037901 (2001). URL <https://link.aps.org/doi/10.1103/PhysRevLett.87.037901>.
- [5] Carusotto, I. & Ciuti, C. Quantum fluids of light. *Reviews of Modern Physics* **85**, 299–366 (2013). [1205.6500](https://doi.org/10.1103/RevModPhys.85.299).
- [6] Muñoz-Matutano, G. *et al.* Emergence of quantum correlations from interacting fibre-cavity polaritons. *Nature Materials* **18**, 213–218 (2019). URL <https://doi.org/10.1038/s41563-019-0281-z>.
- [7] Delteil, A. *et al.* Towards polariton blockade of confined exciton–polaritons. *Nature Materials* **18**, 219–222 (2019). URL <https://doi.org/10.1038/s41563-019-0282-y>.
- [8] Mak, K. F. & Shan, J. Photonics and optoelectronics of 2d semiconductor transition metal dichalcogenides. *Nature Photonics* **10**, 216–226 (2016).
- [9] Zhang, L. *et al.* Van der waals heterostructure polaritons with moiré-induced nonlinearity. *Nature* **591**, 61–65 (2021).
- [10] Alexeev, E. M. *et al.* Resonantly hybridized excitons in moiré superlattices in van der waals heterostructures. *Nature* **567**, 81–86 (2019).
- [11] Zhang, L. *et al.* Twist-angle dependence of moiré excitons in ws 2/mose 2 heterobilayers. *Nature communications* **11**, 1–8 (2020).

- [12] Tang, Y. *et al.* Tuning layer-hybridized moiré excitons by the quantum-confined stark effect. *Nature Nanotechnology* **16**, 52–57 (2021).
- [13] Liu, X. *et al.* Strong light-matter coupling in two-dimensional atomic crystals. *Nature Photonics* **9**, 30–34 (2014). URL <http://dx.doi.org/10.1038/nphoton.2014.304>. 1406.4826.
- [14] Sun, Z. *et al.* Optical control of room-temperature valley polaritons. *Nature Photonics* **11**, 491–496 (2017). URL <https://doi.org/10.1038/nphoton.2017.121>.
- [15] Chen, Y.-J., Cain, J. D., Stanev, T. K., Dravid, V. P. & Stern, N. P. Valley-polarized exciton–polaritons in a monolayer semiconductor. *Nature Photonics* **11**, 431–435 (2017). URL <https://doi.org/10.1038/nphoton.2017.86>.
- [16] Dufferwiel, S. *et al.* Valley-addressable polaritons in atomically thin semiconductors. *Nature Photonics* **11**, 497–501 (2017). URL <https://doi.org/10.1038/nphoton.2017.125>.
- [17] Tan, L. B. *et al.* Interacting polaron-polaritons. *Phys. Rev. X* **10**, 021011 (2020). URL <https://link.aps.org/doi/10.1103/PhysRevX.10.021011>.
- [18] Emmanuele, R. P. A. *et al.* Highly nonlinear trion-polaritons in a monolayer semiconductor. *Nature Communications* **11**, 3589 (2020). URL <https://doi.org/10.1038/s41467-020-17340-z>.
- [19] Kravtsov, V. *et al.* Nonlinear polaritons in a monolayer semiconductor coupled to optical bound states in the continuum. *Light: Science & Applications* **9**, 1–8 (2020).
- [20] Gu, J. *et al.* Enhanced nonlinear interaction of polaritons via excitonic rydberg states in monolayer wse₂. *Nature Communications* **12**, 2269 (2021). URL <https://doi.org/10.1038/s41467-021-22537-x>.
- [21] Rivera, P. *et al.* Observation of long-lived interlayer excitons in monolayer mose₂-wse₂ heterostructures. *Nature communications* **6**, 1–6 (2015).
- [22] Suárez-Forero, D. G. *et al.* Enhancement of parametric effects in polariton waveguides induced by dipolar interactions. *Phys. Rev. Lett.* **126**, 137401 (2021). URL <https://link.aps.org/doi/10.1103/PhysRevLett.126.137401>.

- [23] Togan, E., Lim, H.-T., Faelt, S., Wegscheider, W. & Imamoglu, A. Enhanced interactions between dipolar polaritons. *Phys. Rev. Lett.* **121**, 227402 (2018). URL <https://link.aps.org/doi/10.1103/PhysRevLett.121.227402>.
- [24] Rosenberg, I. *et al.* Strongly interacting dipolar-polaritons. *Science Advances* **4** (2018). URL <https://advances.sciencemag.org/content/4/10/eaat8880>. <https://advances.sciencemag.org/content/4/10/eaat8880.full.pdf>.
- [25] Leisgang, N. *et al.* Giant stark splitting of an exciton in bilayer mos 2. *Nature Nanotechnology* **15**, 901–907 (2020).
- [26] Lorchat, E. *et al.* Excitons in bilayer mos 2 displaying a colossal electric field splitting and tunable magnetic response. *Physical Review Letters* **126**, 037401 (2021).
- [27] Gerber, I. C. *et al.* Interlayer excitons in bilayer mos 2 with strong oscillator strength up to room temperature. *Physical Review B* **99**, 035443 (2019).
- [28] Peimyoo, N. *et al.* Electrical tuning of optically active interlayer excitons in bilayer mos2. *Nature Nanotechnology* 1–6 (2021).
- [29] Deilmann, T. & Thygesen, K. S. Interlayer excitons with large optical amplitudes in layered van der waals materials. *Nano letters* **18**, 2984–2989 (2018).
- [30] Erkensten, D., Brem, S. & Malic, E. Exciton-exciton interaction in transition metal dichalcogenide monolayers and van der waals heterostructures. *Physical Review B* **103**, 045426 (2021).
- [31] Helmrich, S. *et al.* Phonon-assisted intervalley scattering determines ultrafast exciton dynamics in mose₂ bilayers. *Phys. Rev. Lett.* **127**, 157403 (2021). URL <https://link.aps.org/doi/10.1103/PhysRevLett.127.157403>.
- [32] Stepanov, P. *et al.* Exciton-exciton interaction beyond the hydrogenic picture in a mose 2 monolayer in the strong light-matter coupling regime. *Physical Review Letters* **126**, 167401 (2021).
- [33] Byrnes, T., Recher, P. & Yamamoto, Y. Mott transitions of exciton polaritons and indirect excitons in a periodic potential. *Physical Review B* **81**, 205312 (2010).

- [34] Hong, J. *et al.* Exploring atomic defects in molybdenum disulphide monolayers. *Nature communications* **6**, 1–8 (2015).
- [35] Shree, S. *et al.* Interlayer exciton mediated second harmonic generation in bilayer mos2. *Nature communications* **12**, 1–9 (2021).
- [36] Wang, L. *et al.* One-dimensional electrical contact to a two-dimensional material. *Science* **342**, 614–617 (2013).
- [37] Carusotto, I. & Ciuti, C. Quantum fluids of light. *Reviews of Modern Physics* **85**, 299 (2013).

Supplementary Materials: Highly nonlinear dipolar exciton-polaritons in bilayer MoS₂

I Device fabrication

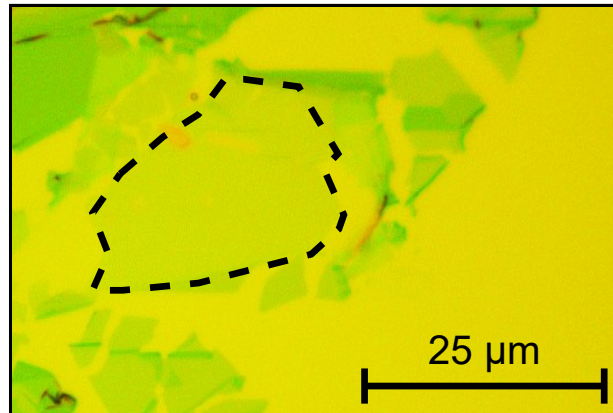


Fig. S1: Optical micrograph of the device. (a) Optical micrograph of the hBN/MoS₂ bilayer/hBN heterostructure on a distributed Bragg reflector (DBR) before top silver mirror deposition. The dashed line marks the uniform area of the heterostructure where measurements are done.

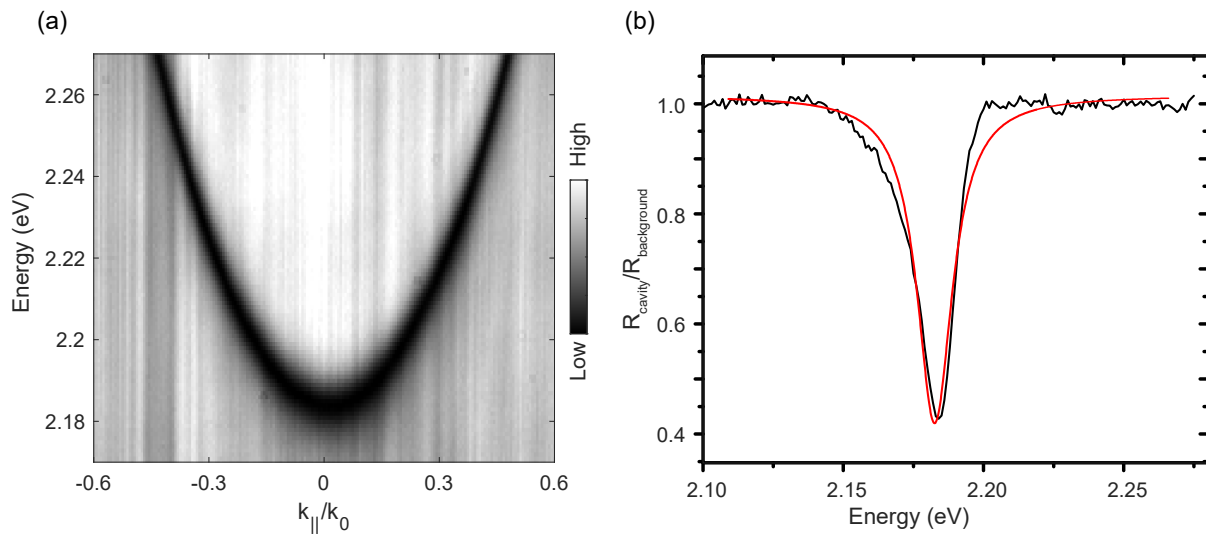


Fig. S2: PMMA bare cavity mode. (a) Dispersion of the PMMA bare cavity mode measured away from the hBN/bilayer MoS₂/hBN heterostructure. The bare cavity mode gets 0.23 eV red shifted on the sample area due to the hBN and bilayer MoS₂. (b) Line cut of the bare cavity mode at $k_{||} = 0$. The red curve is the fitted Lorentzian with a FWHM of 15.5 meV.

II Details of coupled oscillator model

The five polariton branches in our experiment can be described with the eigen modes of the following five coupled oscillator model.

$$\begin{pmatrix} E_{cav} & \Omega_A/2 & \Omega_{IE}/2 & \Omega_{A2s}/2 & \Omega_B/2 \\ \Omega_A/2 & E_A & 0 & 0 & 0 \\ \Omega_{IE}/2 & 0 & E_{IL} & 0 & 0 \\ \Omega_{A2s}/2 & 0 & 0 & E_{A2s} & 0 \\ \Omega_B/2 & 0 & 0 & 0 & E_B \end{pmatrix}$$

where $E_{cav} = \frac{c\hbar}{en_c} \sqrt{k_v^2 + k_{\parallel}^2} = \frac{c\hbar}{en_c} \sqrt{k_v^2 + \left(10^7 \frac{k_{\parallel}}{k_0}\right)^2}$, $k_v = \frac{2\pi}{\lambda_c} n_c$, $k_0 = \frac{2\pi}{\lambda_c} \approx 10^7 \text{ nm}^{-1}$, e is the electronic charge. Here the wavelength is in meter and energy is in eV. The subscripts cav, A, IE, A2s, and B refer to the cavity mode, A exciton, interlayer exciton, 2s state of A exciton, and B exciton respectively. Ω_X and E_X refer to the Rabi splitting and energy of the X exciton respectively.

The fitting yields $\lambda_c = 637.5 \pm 0.1 \text{ nm}$, $n_c = 1.450 \pm 0.003$, $E_{A1s} = 1.9323 \pm 0.0003 \text{ eV}$, $E_{IL} = 2.0014 \pm 0.0001 \text{ eV}$, $E_{A2s} = 2.078 \pm 0.002 \text{ eV}$, $E_B = 2.111 \pm 0.001 \text{ eV}$ and the Rabi splittings $\Omega_{A1s} = 40.4 \pm 0.3 \text{ meV}$, $\Omega_{IL} = 21.4 \pm 0.1 \text{ meV}$, $\Omega_{A2s} = 13 \pm 0.5 \text{ meV}$, $\Omega_B = 51 \pm 0.4 \text{ meV}$.

III Reflection measurements on bare exciton and exciton-polariton data at elevated temperature

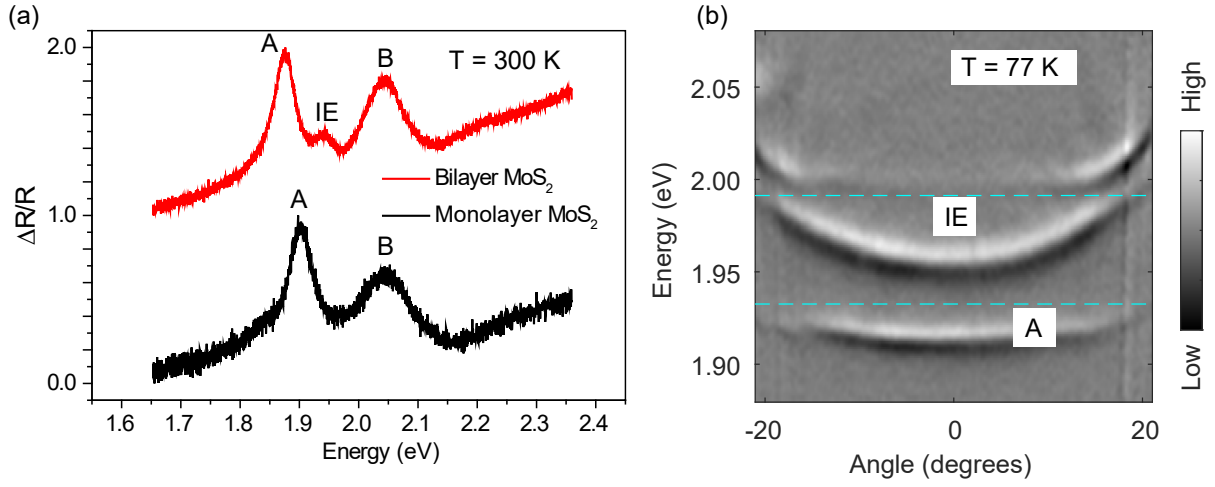


Fig. S3: White light reflection and exciton-polariton at elevated temperatures. (a) The red (black) color plot shows the differential reflection of bilayer (monolayer) MoS₂ on PDMS substrate. The small peak in between the A and B exciton in bilayer is the signature of the IE. (b) Strong coupling of the IE and A exciton at 77 K in bilayer MoS₂.

IV Details of the polariton density calculation

Polariton density is calculated from the Gross-Pitaevskii (GP) equation. The GP equation at wavevector k can be written as

$$i\hbar \frac{\partial \psi_{LP}(k, t)}{\partial t} = \left[\epsilon_{LP}(k) - \frac{i\hbar\gamma_{LP}}{2} \right] \psi_{LP}(k, t) + \hbar F_P(k, t) \quad (S1)$$

Here $\epsilon_{LP}(k) = \hbar\omega_{LP}(k)$ is the energy of the lower polariton of an exciton and γ_{LP} is the line width of the polariton. $F_P(k, t)$ is the coherent driving. The pulse width of our supercontinuum laser is 20 ps which is much larger than the polariton lifetime (30-50 fs). This allows the pumping to be treated as continuous wave which is resonant with our cavity. We can express the pumping term as $F_P(k, t) = F_P(k)e^{-i\omega_P t}$ and $\psi_{LP}(k, t) = \tilde{\psi}_{LP}(k)e^{-i\omega_P t}$ where ω_P is the pump frequency. This simplifies the above equation to

$$\left[\hbar\omega_P - \epsilon_{LP}(k) + \frac{i\hbar\gamma_{LP}}{2} \right] \tilde{\psi}_{LP}(k) = \hbar F_P(k) \quad (S2)$$

The $F_P(k)$ term can be written from the input-output relation.

$$F_P(k) = C(k) \sqrt{\frac{\eta \cdot P_{\text{int}}(k)}{\hbar\omega_P}} \quad (S3)$$

$$\eta = \frac{|t_{\text{top mirror}}|^2}{\tau_{\text{trip}}} \quad (\text{S4})$$

Here $C(k)$ is the photon Hopfield coefficient of the polariton branch. $P_{\text{int}}(k)$ is the incident power on the top mirror and η is the coupling coefficient. $t_{\text{top mirror}}$ is the transmission of top mirror, and τ_{trip} is the photon trip time in the cavity. This gives $\eta = 4.1 \times 10^{12} \text{ s}^{-1}$. Equation S2 can be written as

$$\tilde{\psi}_{LP}(k, \omega_P) = \frac{\hbar F_P(k)}{\hbar \omega_P - \epsilon_{LP}(k) + \frac{i\hbar\gamma_{LP}}{2}} \quad (\text{S5})$$

Polariton density at the wavevector k and frequency ω_P is

$$|\psi_{LP}(k, \omega_P, t)|^2 = \left| \tilde{\psi}_{LP}(k, \omega_P) \right|^2 = \frac{|C|^2 \frac{\eta P_{\text{int}}(k)}{\hbar \omega_P}}{(\omega_P - \omega_{LP}(k))^2 + \left(\frac{\gamma_{LP}}{2}\right)^2} \quad (\text{S6})$$

Since the polaritons have a finite width in energy, the total polariton density at the wavevector k can be found out by integrating over the all frequency range

$$\left| \tilde{\psi}_{LP}(k) \right|^2 = \int \frac{|C|^2 \frac{\eta \cdot \xi(k, \omega_P)}{\hbar \omega_P}}{(\omega_P - \omega_{LP}(k))^2 + \left(\frac{\gamma_{LP}}{2}\right)^2} d\omega_P \quad (\text{S7})$$

Here, $\xi(k, \omega_P)$ denotes the incident power density (power/frequency/wavevector).

The integral above can be numerically calculated but we can make an approximation to get a close form solution for the density. We note that the Lorentzian part of the integrand for $\gamma_{LP} \rightarrow 0$ is a Dirac delta function

$$\delta(\omega_P - \omega_{LP}) = \lim_{\gamma_{LP} \rightarrow 0} \frac{1}{\pi} \frac{\frac{\gamma_{LP}}{2}}{(\omega_P - \omega_{LP})^2 + \left(\frac{\gamma_{LP}}{2}\right)^2} \quad (\text{S8})$$

Using the above formula and taking the power density $\xi(k, \omega_P)$ constant over the narrow range of excitation we get

$$\left| \tilde{\psi}_{LP}(k) \right|^2 \approx \frac{2\pi |C(k)|^2 \eta \cdot \xi}{\hbar \omega_{LP}(k) \gamma_{LP}(k)} \quad (\text{S9})$$

Here, $\gamma_{LP}(k)$ is determined from the experimental data.

Total real space polariton density can be found out by summing $\left| \tilde{\psi}_{LP}(k) \right|^2$ in the k -space for

the experimental wavevector range

$$\begin{aligned} \left| \tilde{\psi}_{LP} \right|^2 &= \sum_{k=k_{min}}^{k_{max}} \left| \tilde{\psi}_{LP}(k) \right|^2 \\ &= \frac{2\pi\eta \cdot \xi}{\hbar} \sum_{k=k_{min}}^{k_{max}} \frac{|C(k)|^2}{\omega_{LP}(k)\gamma_{LP}(k)} \end{aligned} \quad (\text{S10})$$

If P_0 is the measured real space peak power density (power/energy) of the pulsed supercontinuum laser excitation then $\xi = P_0/N$, where N is the number of k point in between k_{min} and k_{max} .

The above equation can also be written as

$$\left| \tilde{\psi}_{LP} \right|^2 = \sum_{k=k_{min}}^{k_{max}} \frac{2\pi}{\omega_{LP}(k) \tau_{trip}} \times \frac{|C(k)|^2 |t_{\text{top mirror}}|^2 R}{\gamma_{LP}(k)} \quad (\text{S11})$$

Here, $\frac{2\pi}{\omega_{LP} \tau_{trip}} \sim 1$ and R is the incident number of photons/sec.

V Raw data for the nonlinearity of the IE polariton

Fig. S4a shows the differential reflection of the IE polaritons excited (with a 20 ps pulsewidth supercontinuum laser) in a narrow band used to study the nonlinearity of the IE polariton. Fig. S4b shows the differential reflection at the zero detuning k_{\parallel} for IE polariton. The upper polariton branch red shifts and lower polariton branch blue shifts with increasing density reducing the Rabi splitting. We also notice that the two branches move asymmetrically – the lower branch moves more than the upper branch at zero detuning k_{\parallel} . This is because both exciton-exciton interaction and saturation give rise to blue shift for the lower branch but they produce opposite shift for the upper branch – as described in the main text.

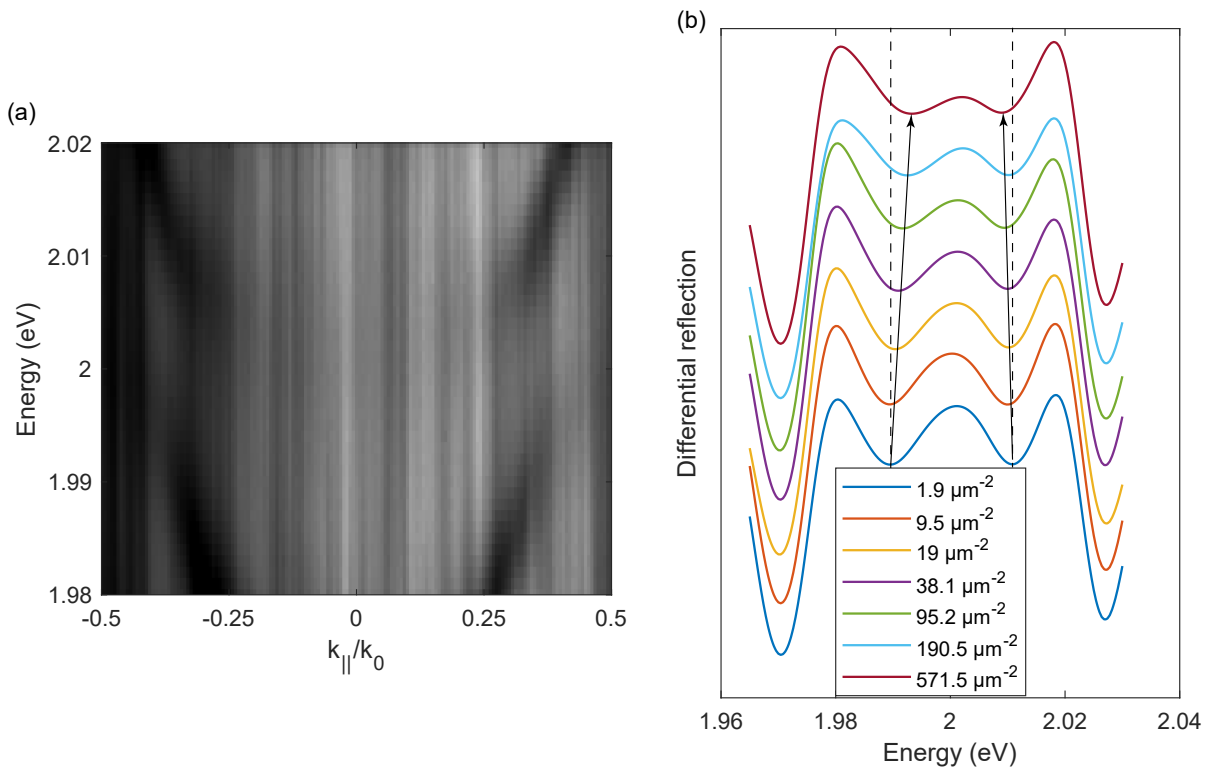


Fig. S4: Raw data for the nonlinearity of the IE polariton at 7 K. (a) K-space differential reflection data showing the dispersion of the IE lower branch (pol-2) and IE upper branch (pol-3) at the lowest density ($1.9 \mu\text{m}^{-2}$). The excitation bandwidth of the supercontinuum laser for the IE is set 40 meV by using a low-pass and a high-pass filter. (b) Line cut of the k-space data at zero detuning $k_{||}$ showing the differential reflection of the IE lower branch (pol-2) and IE upper branch (pol-3) at different polariton density. Note that since the IE exciton blueshifts with increasing density, the zero detuning $k_{||}$ also increases with increasing density. All the power dependent nonlinear measurements (for both samples in the cavity and outside the cavity) were carried out using a pulsed supercontinuum laser (20 ps pulsewidth) with proper bandpass filter in the input to excite only one polariton species.

VI Fits to determine the blueshift of the bare excitons

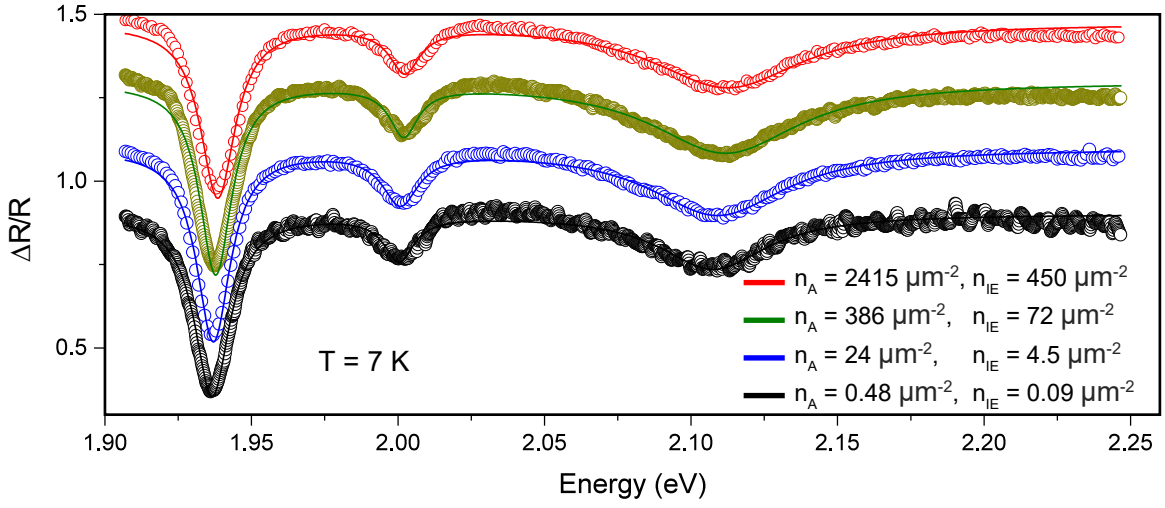


Fig. S5: Power dependent reflectance measurement to measure the blue shift. Three Lorentzian centered at A exciton, IE and B exciton respectively are fitted to the data at each power. The blue shift of the Lorentzians centered at A exciton and IE are plotted in the main text as a function of estimated exciton density. The method of exciton density estimation is described in Methods.

VII Rabi splitting of interlayer exciton polariton as a function of polariton density

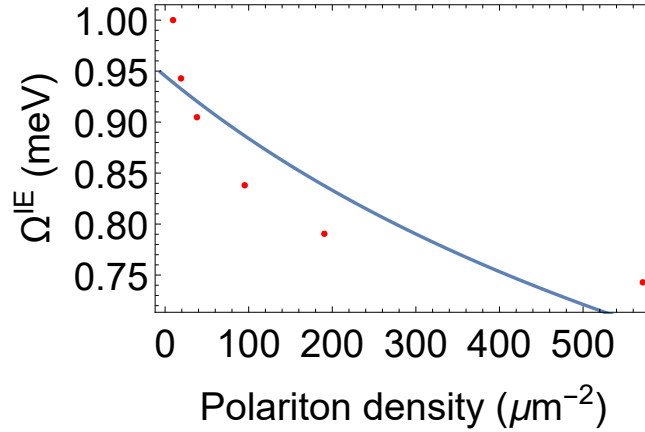


Fig. S6: Rabi splitting of IE polariton at the zero detuning $k_{||}$ as a function of polariton density at 7 K. The blue line is the fit to the usual formula $\Omega = \frac{\Omega_0}{\sqrt{1 + \frac{n}{n_{\text{sat}}}}}$ for free 2D excitons.

We plot the Rabi splitting of the IE polariton at the zero detuning $k_{||}$ as a function of density, see Fig. S6. We note that the usual formula for free 2D excitons $\Omega = \frac{\Omega_0}{\sqrt{1 + \frac{n}{n_{\text{sat}}}}}$ does not fit our data well. The inadequacy of the free 2D exciton formula to describe the density dependence of the Rabi splitting was also observed in a recent study^{S1} on the Moiré exciton-polariton in a hetrobilayer TMDC.

VIII Energy of the lower branch of A exciton polariton as a function of polariton density

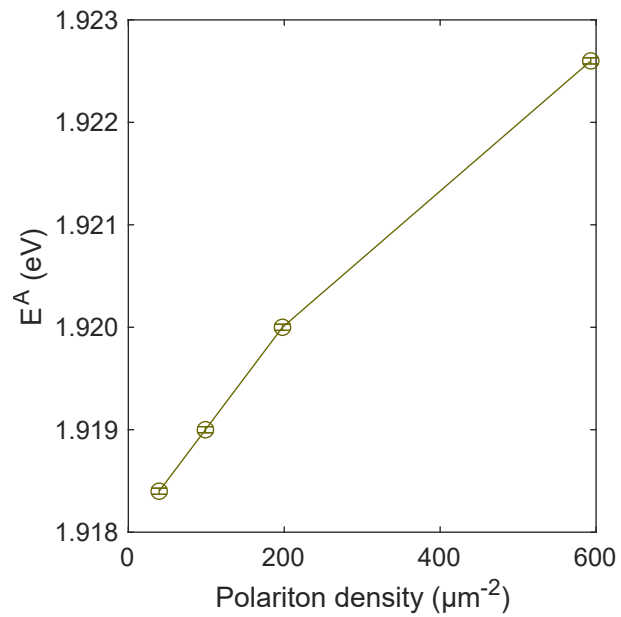


Fig. S7: Energy of the lower branch of A exciton polariton as a function of polariton density at 7 K from which the g_{LP}^A is calculated and plotted in Fig.3b of the main manuscript.

IX Separation of the saturation nonlinearity and exciton-exciton interaction nonlinearity for IE polariton

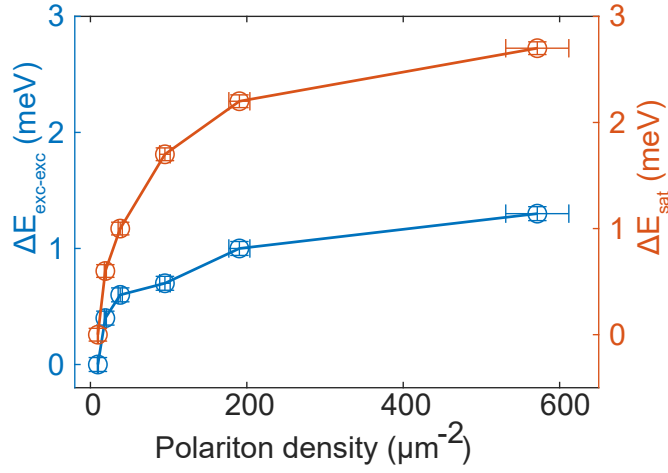


Fig. S8: Separation of the saturation nonlinearity and exciton-exciton interaction nonlinearity for IE polariton. Calculated $\Delta E_{\text{exc-exc}}$ and ΔE_{sat} at the zero detuning k_{\parallel} from the experimental data as a function polariton density.

X Probing non-linearities in the reflectance spectrum of bilayer MoS₂ on two distinct time scales

Fig. S9a shows transient reflectivity measured on the bilayer film. The sample is first excited by an ultrashort pump pulse (200 fs) resonant with one of the exciton transitions. The relative change in reflectivity induced by the pump is then probed as a function of time delay using a broadband pulse. The transient reflectivity spectra obtained when pumping the A, B and IE resonances at a pump-probe delay of 1.5 ps are plotted in Fig. S9b. Regardless of the exciton transition that is initially excited, all the excitonic resonances redshift and saturate (which corresponds to the observed differential lineshapes). Time traces of the transient reflectivity are shown in Fig. S10.

In contrast, we notice that all the excitonic features blueshift when the sample is probed with a single broadband pulse lasting 20 ps (main text Fig. 1d). The opposite shifts observed using these two probes provide insight in the excitation regimes induced in the bilayers. When the probe is delayed from the pump all excitonic features are shifted to lower energies (Fig. S9a). This is consistent with the expected contribution of relaxed carriers in these materials^{S2-S4}. Indeed, the pump-probe delay used in this experiment is much greater than the K-valley exciton lifetime (45 fs for A exciton and 53 fs for IE). In this case, the probe interacts with the sample when only relaxed carriers remain.

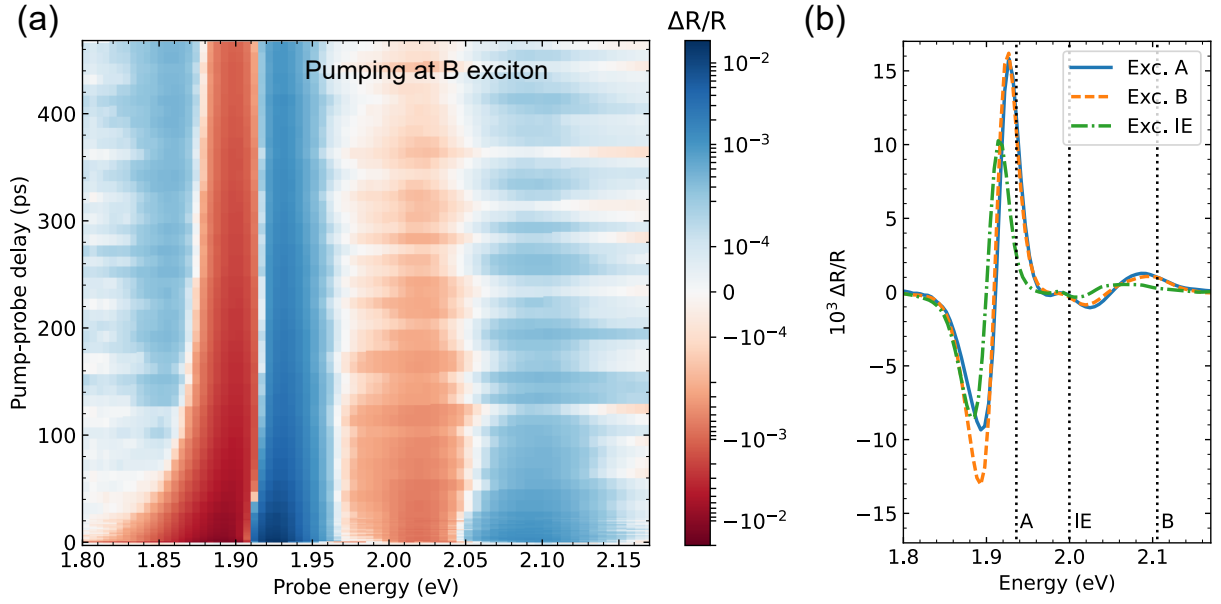


Fig. S9: Probing non-linearities in the reflectance spectrum of bilayer MoS₂ after the excitons scatter from K-valley. (a) Transient reflectivity spectra probed as a function of white-light probe energy and pump-probe delay. (b) Transient reflectivity spectra probed 1.5 ps after the resonant excitation of the A (full), B (dashed) and IE (dot-dashed) excitons. The absorbed photon density is about 4×10^4 photons/ μm^2 , 2×10^4 photons/ μm^2 and 4×10^4 photons/ μm^2 respectively.

When the reflectivity is probed while the material is still being pumped, as is the case in the single pulse reflectivity experiment, the dominant non-linear effect is instead a shift of all features to higher energies. Indeed, when the pulse interacts with the sample, A, B and IE excitons are continuously created while their constituents quickly relax out of the K valley. This quasi-continuous pumping leads to the steady-state presence of A, IE and B excitons amidst a growing background of relaxed carriers until the pulse no longer interacts with the sample. Moreover, the blueshift arising from excitonic repulsion dominates over the (smaller) redshift from the background of relaxed carriers. Given the long pulses used in our single pulse reflectivity, compared to the lifetime of the excitons (~ 50 fs), there are about $20 \text{ ps}/50 \text{ fs} = 400$ times more relaxed carriers than excitons. The strength of the K-valley exciton-exciton interactions are therefore much higher than that due to the interaction with the background carriers.

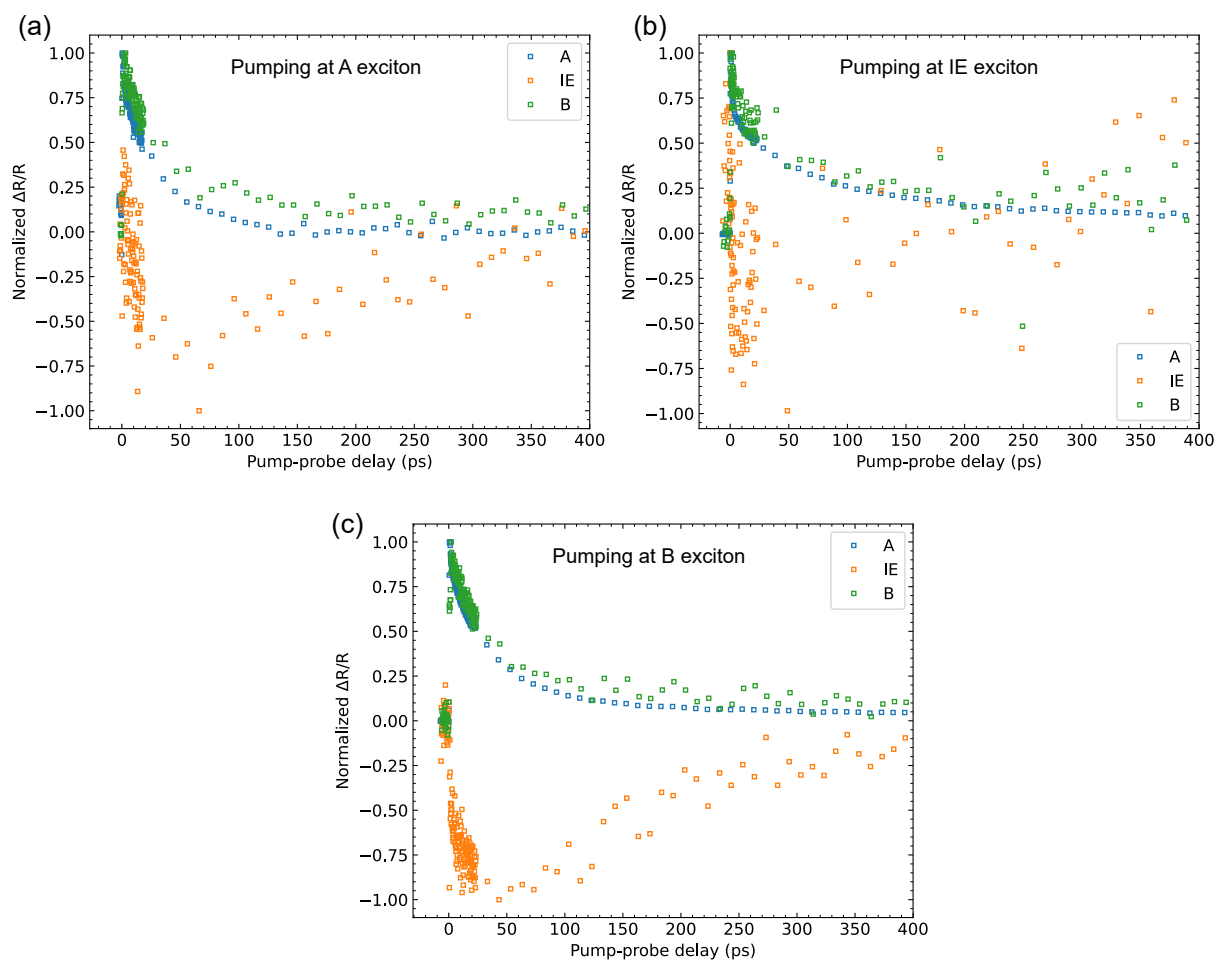


Fig. S10: Probing non-linearities in the reflectance spectrum of bilayer MoS₂ after the excitons scatter from K-valley. Transient reflectivity spectra probed as a function of white-light probe energy and pump-probe delay. The legend corresponds to the probe exciton energy where the time trace is taken.

References

- [S1] Zhang, L. *et al.* Van der waals heterostructure polaritons with moiré-induced nonlinearity. *Nature* **591**, 61–65 (2021).
- [S2] Schmidt, R. *et al.* Ultrafast coulomb-induced intervalley coupling in atomically thin ws2. *Nano letters* **16**, 2945–2950 (2016).
- [S3] Steinhoff, A., Rosner, M., Jahnke, F., Wehling, T. O. & Gies, C. Influence of excited carriers on the optical and electronic properties of mos2. *Nano letters* **14**, 3743–3748 (2014).
- [S4] Sie, E. J. *et al.* Observation of exciton redshift–blueshift crossover in monolayer ws2. *Nano letters* **17**, 4210–4216 (2017).